BUTTERWORTH HEINEMANN

Conjugate natural convection from an array of discrete heat sources: part 1 — two- and three-dimensional model validation

T. J. Heindel, S. Ramadhyani, and F. P. Incropera
Heat Transfer Laboratory, School of Mechanical Engineering, Purdue University, West Lafayette, IN, USA

Two- and three-dimensional (2- and 3-D) numerical models have been developed for conjugate natural convection in a discretely heated cavity. Experimental results obtained for the same geometry, using water and FC-77 as the coolants, were in excellent agreement with the 3-D numerical predictions. In contrast, because of the inability to account for thermal spreading in the lateral direction, the 2-D model overpredicted measured average surface temperatures of the discrete heat sources. However, the 2-D model still predicted general trends and flow patterns that were experimentally obtained. The nature and extent of 3-D effects on the flow and heat transfer have been delineated.

Keywords: natural convection; conjugate heat transfer; numerical and experimental comparisons; electronic cooling

Introduction

Continued miniaturization of integrated circuits on a single computer chip and reduced spacing of chips in an array have contributed to significant improvements in the performance of computer systems. However, increased circuit densities require larger power dissipation and complicate thermal control when a principal objective is to maintain components at or below specified maximum service temperatures (Peterson and Ortega 1990). Currently, thermal control typically is maintained by direct air cooling or by indirect liquid or air cooling (Incropera 1988, 1990; Bar-Cohen 1991). However, implementation of such cooling schemes for a powerful work station or desktop computer would require a coolant distribution system that includes a fan or pump and associated duct or plumbing fixtures. Undesirable noise and vibration may accompany the fan or pump assembly.

In contrast, natural convection affords a means of thermal control that eliminates the fan or pump and provides a noise- and vibration-free environment. Because relatively low convective heat transfer coefficients are associated with natural convection from small heat sources (computer chips) mounted in a substrate (printed circuit board), conduction through the substrate influences the heat transfer process. Conjugate heat transfer involves the coupling of conduction in a solid and convection in a fluid. The coupling allows for thermal spreading to occur through the substrate and provides an additional heat transfer path from the heat source to the fluid. Analyses of natural convection heat transfer from discrete heat sources typically ignore conjugate heat transfer effects and utilize idealized thermal conditions at the solid/fluid interface. Additionally, many previous investigations involving natural convection from discretely heated cavities assume that the geometry and resulting flow and heat transfer can be approximated as two-dimensional (2-D). Therefore, discrete rectangular heat sources are approximated as long strip heaters for which the dimension L_x (see Figure 1) is taken to be very large. The present study avoids these assumptions by developing 2-D and three-dimensional (3-D) conjugate models to predict flow and heat transfer within a discretely heated cavity. Experimental measurements and flow visualization were also obtained from small heat sources and compared to the numerical predictions.

Various numerical studies involving conduction in a solid region and natural convection in a discretely heated cavity have been performed by Joshi and co-workers. Sathe and Joshi (1991) investigated 2-D conjugate natural convection from a substrate-mounted heat generating protrusion suspended in the central region of a cavity. Prandtl number effects were negligible for $10 \leq \mathrm{Pr} \leq 1000$, and substrate conduction decreased with increasing Rayleigh number. For a fixed Rayleigh number of 10^6, substrate conduction was the dominant path for heat transfer from the heated protrusion to the fluid when $R_s > 10$. Therefore, in most applications, substrate conduction effects cannot be neglected. Sathe and Joshi (1992) extended this study to account for the thermal conductivity of the protrusion as well as the geometries of the substrate and protrusion. Joshi et al. (1993) considered a discrete heat source flush mounted to the substrate, and similar trends were predicted.

Wroblewski and Joshi (1992, 1993, 1994) performed an extensive 3-D conjugate natural convection study for a single, protruding heat source mounted to a substrate that forms one wall of a cubical cavity. At a low Rayleigh number ($\mathrm{Ra}_L = 10^3$) and a high substrate/fluid thermal conductivity ratio ($R_s = 575$), the fluid flow and isotherms resemble those associated with a differentially heated cavity. In general, conduction through the substrate played an important role in reducing the maximum temperature of the discrete heat source when $R_s > 10$.

Polentini et al. (1993) completed an extensive experimental study involving a 3-D enclosure. A 3×3 heater array was flush mounted on one wall, with the opposing wall isothermally cooled. The Nusselt number was found to be independent of aspect ratio

Address reprint requests to T. J. Heindel, Institute of Paper Science and Technology, 500 10th Street NW, Atlanta, GA 30318-5794, USA.

Received 10 March 1995; accepted 10 July 1995

Int. J. Heat and Fluid Flow 16: 501–510, 1995

655 Avenue of the Americas, New York, NY 10010

0142-727X/95/$10.00
SSDI 0142-727X(95)00058-X

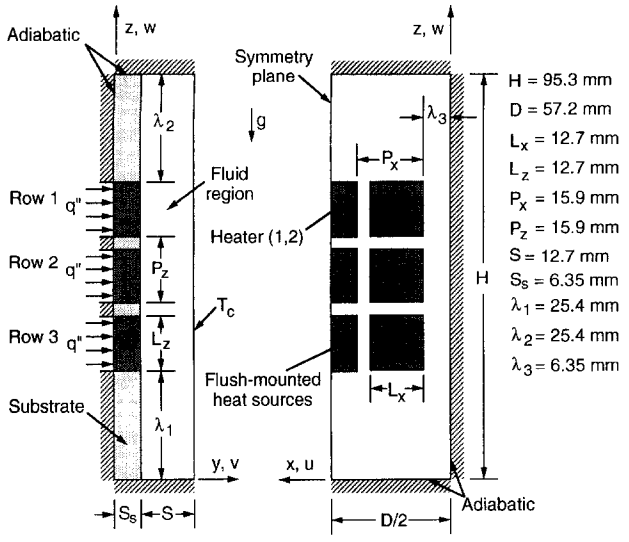

Figure 1 Numerical and experimental geometry and nomenclature

($2.5 \leq A_z \leq 7.5$) and Prandtl number ($5 \leq \mathrm{Pr} \leq 25$). Additional studies addressing natural convection from small heat sources mounted in a cavity have been completed, and these results are summarized in the review papers by Jaluria (1985), Incropera (1988, 1990), Peterson and Ortega (1990), and Bar-Cohen (1993).

This paper numerically and experimentally investigates the coupled conduction and natural convection transport from an array of discrete, isoflux heat sources flush mounted to one vertical wall of a cavity. The opposite vertical wall and the horizontal walls are assumed to be isothermal and adiabatic, respectively. The thermal conditions at the heater/fluid and substrate/fluid interfaces are not known a priori but are determined through the solution process. Two different fluids were simulated in the calculations, which matched those used in the experiment, water (Pr = 5) and FC-77 (a dielectric fluorocarbon liquid with Pr = 25). Numerical predictions for $\mathrm{Ra}^*_{L_z} \leq 10^9$ were obtained with a 2-D and 3-D conjugate model and were compared to experimental data and flow visualization. A major objective of this paper is to elucidate the nature and extent of 3-D effects on both the flow and heat transfer. In a companion paper (Heindel et al. 1995), the 2-D conjugate model is used in a detailed study of parametric effects.

Numerical model

Figure 1 displays a schematic of the geometry modeled in the 3-D numerical predictions, which was selected to match that of the experimental apparatus. One vertical wall is composed of a 3×3 array of discrete heat sources mounted in a substrate of different thermal conductivity. An isoflux condition is imposed at the back of each heat source, while the back of the substrate is assumed to be adiabatic. The opposite wall is maintained isothermal, and the remaining walls are assumed adiabatic. These boundary conditions, including the isoflux heater boundary condition, were chosen to simulate experimental conditions. Because symmetry was observed in previous fully 3-D calculations (Wroblewski and Joshi 1992, 1994), a plane of symmetry at $x = D/2$ is used to reduce the computational domain by a factor of two.

Governing equations

Assuming steady-state heat transfer with constant thermal physical properties, negligible contact resistance between the heater/substrate interface, laminar natural convection with no viscous dissipation, and the Boussinesq approximation, the dimensionless governing equations for the fluid and solid regions can be written as follows:

Notation

A_{htr}	heater aspect ratio, L_x/L_z
A_x	minor aspect ratio, D/S
A_z	major aspect ratio, H/S
D	cavity dimension along the x-axis
g	gravitational acceleration
H	cavity dimension along the z-axis
k_f	fluid thermal conductivity
k_h	heater thermal conductivity
k_s	solid thermal conductivity
L_x	heater length in the x-direction
L_z	heater length in the z-direction
P	dimensionless pressure, $p/\rho(\alpha_f/L_z)^2$
Pr	Prandtl number, ν/α_f
P_x	heater pitch in the x-direction
P_z	heater pitch in the z-direction
p	pressure
q''	applied (measured) heat flux
$\hat{q}''$	dimensionless heat flux at the solid/fluid interface, $q''\|_i/q''$
$q''\|_i$	local heat flux at the solid/fluid interface
$\mathrm{Ra}^*_{L_z}$	modified Rayleigh number, $g\beta q'' L_z^4/(k_f \alpha_f \nu)$
R_h	heat source/fluid thermal conductivity ratio, k_h/k_f
R_s	substrate/fluid thermal conductivity ratio, k_s/k_f
S	cavity dimension along the y-axis
S_s	substrate thickness
T	temperature
T_c	cold plate temperature
U, V, W	dimensionless velocity components; e.g., uL_z/α_f
u, v, w	velocity components
X, Y, Z	dimensionless coordinates; e.g., x/L_z
x, y, z	coordinate directions

Greek

α_f	fluid thermal diffusivity
β	volumetric thermal expansion coefficient
Γ	solid region diffusion coefficient
θ	dimensionless temperature, $(T - T_c)/(q'' L_z/k_f)$
λ_i	distances, refer to Figure 1
ν	kinematic viscosity
ρ	fluid density
Ψ	dimensionless stream function

Subscripts

(i, j)	heater (i, j)
sur	surface

Fluid:

Continuity:

$$\frac{\partial U}{\partial X}+\frac{\partial V}{\partial Y}+\frac{\partial W}{\partial Z}=0 \tag{1}$$

Momentum:

$$U\frac{\partial U}{\partial X}+V\frac{\partial U}{\partial Y}+W\frac{\partial U}{\partial Z}=\mathrm{Pr}\left[\frac{\partial^2 U}{\partial X^2}+\frac{\partial^2 U}{\partial Y^2}+\frac{\partial^2 U}{\partial Z^2}\right]-\frac{\partial P}{\partial X} \tag{2}$$

$$U\frac{\partial V}{\partial X}+V\frac{\partial V}{\partial Y}+W\frac{\partial V}{\partial Z}=\mathrm{Pr}\left[\frac{\partial^2 V}{\partial X^2}+\frac{\partial^2 V}{\partial Y^2}+\frac{\partial^2 V}{\partial Z^2}\right]-\frac{\partial P}{\partial Y} \tag{3}$$

$$U\frac{\partial W}{\partial X}+V\frac{\partial W}{\partial Y}+W\frac{\partial W}{\partial Z}=\mathrm{Pr}\left[\frac{\partial^2 W}{\partial X^2}+\frac{\partial^2 W}{\partial Y^2}+\frac{\partial^2 W}{\partial Z^2}\right]-\frac{\partial P}{\partial Z}+\mathrm{Ra}^*_{L_z}\,\mathrm{Pr}\,\theta \tag{4}$$

Energy:

$$U\frac{\partial \theta}{\partial X}+V\frac{\partial \theta}{\partial Y}+W\frac{\partial \theta}{\partial Z}=\frac{\partial^2 \theta}{\partial X^2}+\frac{\partial^2 \theta}{\partial Y^2}+\frac{\partial^2 \theta}{\partial Z^2} \tag{5}$$

Solid:

Energy:

$$0=\Gamma\left[\frac{\partial^2 \theta}{\partial X^2}+\frac{\partial^2 \theta}{\partial Y^2}+\frac{\partial^2 \theta}{\partial Z^2}\right] \tag{6}$$

where

$$X=\frac{x}{L_z} \qquad Y=\frac{y}{L_z} \qquad Z=\frac{z}{L_z} \tag{7}$$

$$U=\frac{uL_z}{\alpha_f} \qquad V=\frac{vL_z}{\alpha_f} \qquad W=\frac{wL_z}{\alpha_f} \tag{8}$$

$$P=\frac{p}{\rho(\alpha_f/L_z)^2} \qquad \theta=\frac{T-T_c}{(q''L_z/k_f)} \tag{9}$$

$$\mathrm{Pr}=\frac{\nu}{\alpha_f} \qquad \mathrm{Ra}^*_{L_z}=\frac{g\beta q'' L_z^4}{k_f \alpha_f \nu} \tag{10}$$

$$R_s=\frac{k_s}{k_f} \qquad R_h=\frac{k_h}{k_f}$$

$$\Gamma=\begin{cases} R_h & \text{in the heater region} \\ R_s & \text{in the substrate region} \end{cases} \tag{11}$$

Note that the modified Rayleigh number is based on the heater length and the isoflux condition applied at the heater. The governing equations for 2-D flow and heat transfer can be obtained from the above equations with $U=(\partial/\partial X)=(\partial^2/\partial X^2)=0$.

Boundary conditions

All the calculations assumed symmetry about the plane defined at $x=D/2$, allowing the computational domain to be reduced by a factor of two. The resulting boundary conditions at the enclosure walls and the plane of symmetry are as follows:

- *At* $X=0$:

$$U=V=W=0 \tag{12}$$

$$\frac{\partial \theta}{\partial X}=0 \tag{13}$$

- *At* $X=\dfrac{D}{2L_z}$:

$$U=\frac{\partial V}{\partial X}=\frac{\partial W}{\partial X}=0 \tag{14}$$

$$\frac{\partial \theta}{\partial X}=0 \tag{15}$$

- *At* $Y=0$:

$$U=V=W=0 \tag{16}$$

$$\frac{\partial \theta}{\partial Y}=\begin{cases} \dfrac{-1}{R_h} & \text{at the heater} \\ 0 & \text{at the substrate} \end{cases} \tag{17}$$

- *At* $Y=\dfrac{S}{L_z}$:

$$U=V=W=0 \tag{18}$$

$$\theta=0 \tag{19}$$

- *At* $Z=0$ *and* $Z=\dfrac{H}{L_z}$:

$$U=V=W=0 \tag{20}$$

$$\frac{\partial \theta}{\partial Z}=0 \tag{21}$$

Consistency of temperatures and heat fluxes at the interfaces between regions of dissimilar materials are explicitly ensured in the numerical solution by using the harmonic mean formulation for the interface conductivities (Patankar 1980).

Solution procedure

The governing equations are discretized using the control–volume formulation described by Patankar (1980), where the velocity control volumes are staggered with respect to the pressure and temperature control volumes. The resulting algebraic equations are then iteratively solved using a line-by-line application of the tridiagonal matrix algorithm enhanced by an additive-correction multigrid method to speed convergence. Coupling of the pressure and velocity fields is treated via the SIMPLER algorithm (Patankar 1980). It is noted that, although separate equations are written for the fluid and solid regions, numerical solutions are obtained in both regions simultaneously by solving the continuity, momentum, and energy equations in the entire computational domain. By specifying the appropriate thermophysical properties in each region, the governing equations are reduced to the appropriate forms for each of the two regions. A degenerate form of the momentum equations, obtained by assigning very large viscosities, is solved in the solid region (Patankar 1978).

Use of the additive-correction multigrid method was necessitated by the large discontinuities in thermophysical properties within the solution domain. Originally, the line-by-line block correction procedure presented by Patankar (1981) was adopted, where corrections are alternately applied along lines of constant X, Y, and Z. Because of the large discontinuities in thermophysical properties, this procedure produced corrections that were appropriate in one region, but inappropriate in others. These inappropriate corrections, particularly to the energy equation in

the solid regions, prevented the realization of converged solutions at all but the lowest modified Rayleigh numbers. Similar nonconvergence problems are briefly mentioned in other natural convection conjugate analyses (Sathe and Joshi 1991, 1992; Joshi et al. 1993; Wroblewski and Joshi 1993).

To overcome the foregoing problem, the additive-correction multigrid (ACM) procedure described by Hutchinson and Raithby (1986) and Hutchinson et al. (1988) was implemented. This procedure allows for N grid levels in the computational domain, where the solution to the finest grid equations provides the solution to the original discretized governing equations. Correction equations on successively coarser grids provide the corrections that are applied to the preceding finer grid equations.

In the present study, a $32 \times 40 \times 80$ ($X \times Y \times Z$) nonuniform fine grid was used to generate the solution to the governing equations, and two additional coarse grids were used to generate grid correction factors. In the limit of a converged solution, the grid correction factors approached zero. Care was taken in the deployment of all grid levels to ensure that all interfaces of discontinuity in the material properties were represented by grid control surfaces. For example, the solid/fluid and heater/substrate interfaces were prescribed as control surfaces at every grid level. This procedure prevented the same correction from being applied over different material regions. The ACM method provided solutions at modified Rayleigh numbers as high as 10^9.

The overall solution algorithm used in this study involved initially obtaining a 2-D solution at a modified Rayleigh number for which heat transfer is conduction dominated ($\mathrm{Ra}^*_{L_z} = 10^4$). This solution was then used as input to 2-D calculations at the next higher modified Rayleigh number of interest. This process continued until $\mathrm{Ra}^*_{L_z} = 10^9$. Steady-state solutions were obtained at each modified Rayleigh number using under-relaxation techniques. Only the momentum equations were under-relaxed by a relaxation factor of 0.85 for the initial solution. As the modified Rayleigh number was increased, the momentum equation relaxation factors were slowly decreased. The solutions from the 2-D calculations were then used as input at all x-plane locations for the 3-D calculations, with $U(x, y, z)$ initialized to zero. The X-component momentum equation was also under-relaxed in the 3-D calculations, but did not require as much under-relaxation as the other momentum equations. Under-relaxation of the energy equation was also used in the 3-D calculations at higher modified Rayleigh numbers, with relaxation factors typically on the order of 0.95.

Solutions were deemed to be converged after three criteria were satisfied. First, the maximum mass source, when compared to the maximum mass flux across a fine-grid control surface, was required to be below 10^{-3}. Second, the iteration-to-iteration change was examined at every fine-grid nodal point for all calculated values. However, to reduce the likelihood of false convergence related to small, but persistent changes between successive iterations due to under-relaxation, the examinations were implemented between iterations i and $i - 20$. The change in computed value, when compared to the maximum value in the domain, was required to be less than 0.5% for a converged solution to be realized. Finally, the overall energy balance was required to be satisfied to within 1%. Typically, the second criterion was the last to be satisfied.

The numerical codes and procedure were validated (Heindel 1994) by obtaining excellent agreement with the benchmark results for natural convection in differentially heated 2-D (de Vahl Davis 1983) and 3-D (Fusegi et al. 1991) cavities.

Even with the added ACM method to speed convergence, the 3-D conjugate calculations still required a very substantial computational effort. For example, all of the calculations satisfied the outlined convergence criteria, with the exception of the FC-77 predictions at $\mathrm{Ra}^*_{L_z} = 10^9$. These calculations satisfied all criteria except the energy balance, which was fulfilled to within 2.1% instead of 1%. Even with this less restrictive convergence criterion, a large amount of CPU time was required (over 5500 CPU minutes on an IBM 3090 computer).

In view of the sizable computational effort involved in the 3-D conjugate calculations, only a partial, 2-D grid-independence study was performed. To ensure grid independence, grid studies should be performed at the highest modified Rayleigh number where the velocity and thermal boundary layers are thinnest. Initial grid studies were performed in the fluid region, before the conjugate calculations were begun, to ensure the boundary layers were satisfactorily resolved (Heindel 1994). By increasing the fluid region grid size from 30×68 to 40×96, the average heat transfer rate on each heated surface changed by at most 2%. Therefore, the 30×68 grid provided a good compromise between computational effort and accuracy in the fluid region. For the conjugate calculations, the grid size in the fluid region was changed to 29×80 because of requirements imposed by the ACM grid deployments. In the Y-direction, fluid region nodes were deployed in the same manner as those in the grid study. An additional 11 nodes were deployed in the Y-direction in the solid region. Although auxiliary grid studies were not performed for the conjugate calculations, the resulting 40×80 grid was deemed sufficient to capture the physics in the fluid and allow for thermal spreading in the solid. The grid deployment scheme used over the heater array in the Z-direction was then used over the heater array in the X-direction for the 3-D calculations, resulting in a 3-D grid size of $32 \times 40 \times 80$.

Experimental methods

For brevity, the experimental methods are summarized. Details can be found in Heindel (1994). The test cell dimensions correspond to those outlined in Figure 1. The test cell, shown schematically in Figure 2, consisted of a 3×3 array of copper elements flush mounted in a G-10 fiberglass substrate, an opposing cold plate, and a Lexan spacer plate compressed between two aluminum clamping plates by bolts passing through each corner and nylon-tipped thumb screws periodically located about the perimeter. O-rings were used to seal the interfaces between components. Two threaded holes were located near the top of the substrate to allow for filling and draining of the test cell. A length of polyethylene tubing, with the free end open to the atmosphere, was attached to each hole through a tube fitting to allow for fluid expansion.

Each heater was formed by a 12.7 mm $\times$ 12.7 mm $\times$ 9.5 mm oxygen-free copper block, forming a square heater face ($A_{\mathrm{htr}} = 1.0$). Two surface-mounted copper-constantan thermocouples were soft-soldered to the copper surface to provide intimate thermal contact. The substrate around each block was beveled

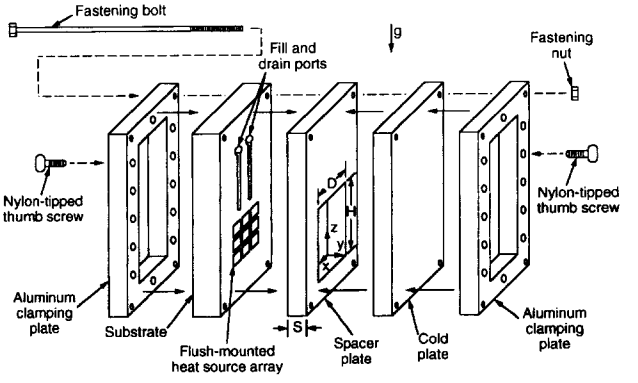

Figure 2 Schematic of the experimental test cell assembly

and filled with red RTV silicone sealant to provide a seal between the copper block and the substrate. Thick-film resistive elements, each powered individually by a dc power source, were soldered to the back of each copper block, forming the discrete heat source. A small cavity behind the heater array was filled with Sylox insulating material ($k_{\text{Sylox}} = 0.02$ W/mK) to minimize environmental losses.

One of two water-cooled cold plates was located opposite the heater array. A copper cold plate was employed for data collection and flow visualization in the y–z plane. Because of the large thermal conductivity of copper, this wall was nearly isothermal and maintained at $T_c \approx 15$°C. The plate contained an internal maze of channels through which water from a constant temperature bath could be circulated. The cold plate surface temperature was measured via three copper–constantan surface-mounted thermocouples. A clear glass cold plate, whose design is detailed in Heindel (1994), was used for flow visualization in the x–z plane.

The spacer plate was fixed at $S = 12.7$ mm, providing a cavity major and minor aspect ratio of $A_z = 7.5$ and $A_x = 4.5$, respectively. Experiments were conducted with degassed, deionized water and degassed FC-77. All heaters were equally powered, and steady-state temperatures and power inputs were recorded by a HP data acquisition system interfaced to a personal computer.

Flow visualization studies were also conducted by suspending small-diameter pliolite particles in degassed, deionized water. These particles had such a small settling rate in water that it was assumed that they closely followed the fluid motion. After a predetermined test condition was reached, the particles in a desired plane were illuminated by a thin sheet of light produced from a 10 mW helium–neon laser, which was introduced into the cavity through the bottom of the enclosure. Time-lapse photographs were then taken of the particle streaks to obtain qualitative flow field information.

All tests were conducted under conditions of equal power dissipation, which was determined by using the HP data acquisition system to measure the current through, and the voltage across, the thick-film resistive element. Hence, the applied heat flux was experimentally measured. Steady-state surface temperatures on the copper heaters and the cold plate were also recorded. These measurements facilitated direct comparisons between experimental values and numerical predictions.

Estimated maximum uncertainties in the reported applied powers and temperature differences, as computed by the procedure described by Kline and McClintock (1953), were 7.0 and 5.0%, respectively.

Results

Numerical predictions

The 3-D conjugate model employed the physical dimensions of the experimental test facility, and the 2-D conjugate model utilized a 2-D approximation of this geometry. The thermophysical properties of the substrate and heater were prescribed to match those of G-10 fiberglass ($k_s \approx 0.29$ W/mK) and copper ($k_h \approx 400$ W/mK). Two different fluids were simulated in the calculations, water (Pr = 5) and FC-77 (Pr = 25), while all other parameters were held constant. These characteristics provided for conductivity ratios of $R_h = 650$ and $R_s = 0.48$ for water, and $R_h = 6420$ and $R_s = 4.7$ for FC-77. Because R_h is large for both fluids, the sole effect of R_s can be addressed. Calculations were performed over a range of modified Rayleigh numbers, based on the heat flux applied at the back of each heater ($10^5 \le \text{Ra}^*_{L_z} \le 10^8$ for water and $10^5 \le \text{Ra}^*_{L_z} \le 10^9$ for FC-77), encompassing values considered experimentally.

Altering the substrate/fluid thermal conductivity ratio has a significant effect on the shape of the vertical velocity profile in a discretely heated cavity. Two such profiles at the trailing edge of row one ($z/L_z = 5.5$) are shown in Figure 3 for $\text{Ra}^*_{L_z} = 10^5$. The darkened regions along the x-axis at $y/L_z = 0$ mark the locations of the heater columns, and the solid/fluid interface is located at $y/L_z = 0.5$. The effect of discrete heater columns is evident in the water calculations (Figure 3a), but is difficult to discern from the ascending flow pattern for FC-77 (Figure 3b). The projected velocity contours also display nearly uniform flow across the heated wall when $R_s = 4.7$ (Figure 3b). Collectively, Figures 3a and 3b reveal that the three-dimensionality of the flow field is muted as R_s increases. As expected, the isothermal cold plate produces a uniform descending vertical velocity in the x-direction at $y/L_z = 1.5$.

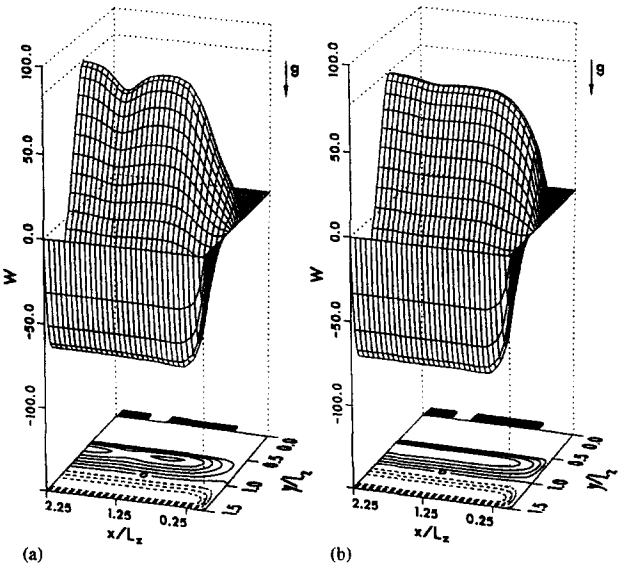

Figure 3 The W velocity profile at $z/L_z = 5.5$ (trailing edge of row one) for $\text{Ra}^*_{L_z} = 10^5$: (a) Pr = 5.0, $R_h = 650$, $R_s = 0.48$ (water); (b) Pr = 25, $R_h = 6420$, $R_s = 4.7$ (FC-77)

Increasing the modified Rayleigh number to 10^8 (Figure 4) increases the vertical velocity. The boundary layers are also much thinner along the heated and cooled walls, and the vertical

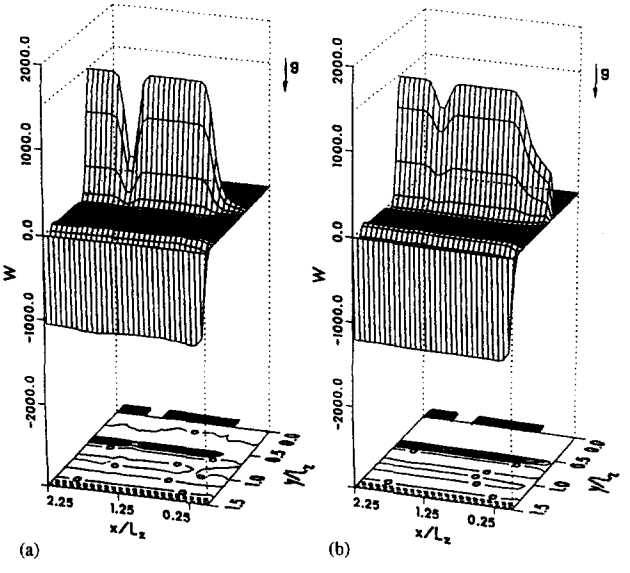

Figure 4 The W velocity profile at $z/L_z = 5.5$ (trailing edge of row one) for $\text{Ra}^*_{L_z} = 10^8$: (a) Pr = 5.0, $R_h = 650$, $R_s = 0.48$ (water); (b) Pr = 25, $R_h = 6420$, $R_s = 4.7$ (FC-77)

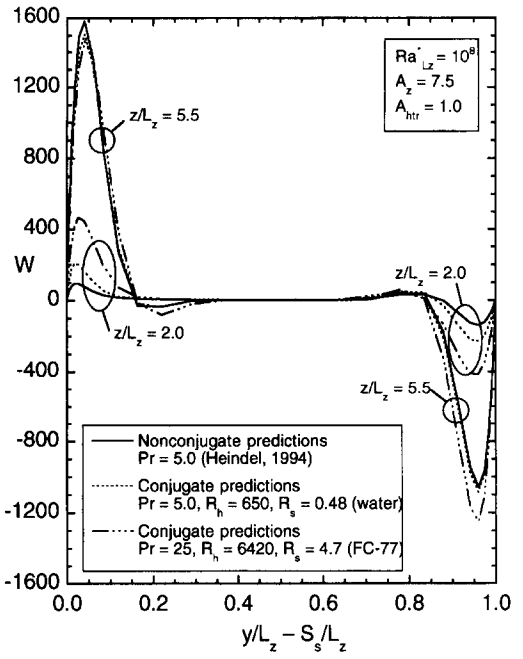

Figure 5 W velocity profiles at the plane of symmetry ($x/L_z = 2.25$) and $z/L_z = 2.0$ and $z/L_z = 5.5$ for $Ra^*_{L_z} = 10^8$

velocity is nearly zero across a wide central region of the cavity, indicating a stagnant core. The larger convection coefficients along the heater face, associated with the increased $Ra^*_{L_z}$, also inhibit thermal spreading throughout the substrate, accentuating the effects of discrete heating by restricting the development of the ascending vertical velocity profile in the substrate regions, particularly for water.

Velocities predicted by the two different 3-D conjugate simulations, as well as for 3-D nonconjugate predictions from Heindel (1994), are compared in Figure 5 by focusing on profiles associated with the plane of symmetry ($x/L_z = 2.25$) and the leading edge of row three ($z/L_z = 2.0$) and the trailing edge of row one ($z/L_z = 5.5$). Near the hot wall ($y/L_z - S_s/L_z = 0$) and at $z/L_z = 2.0$, dimensionless velocities predicted by the FC-77 conjugate simulations are maximum, while velocities predicted by the nonconjugate simulations for water are minimum. In the conjugate calculations with $R_s = 4.7$, thermal spreading occurs through the substrate and energy enters the fluid through the substrate/fluid interface below the heater array. This transport produces a buoyant force below the heaters, inducing fluid motion in this region. When this fluid reaches row three, buoyant forces adjacent to the heat source increase the fluid momentum, causing velocities to exceed those predicted by the nonconjugate model.

The foregoing trends are reversed farther up the heated wall, as indicated at $z/L_z = 5.5$. In this region, maximum and minimum velocities are predicted by the nonconjugate and FC-77 conjugate simulations, respectively. However, the differences in the predicted velocities are small.

Near the cold wall ($y/L_z - S_s/L_z = 1$), maximum descending vertical velocities are predicted at both z/L_z locations when $R_s = 4.7$, and minimum velocities are predicted by the nonconjugate model. This trend is caused by thermal spreading in the substrate to the lower regions of the cavity, activating fluid motion in this region and increasing the overall fluid circulation (mass flow rate). This behavior is also highlighted in the companion paper (Heindel et al. 1995), which addresses only 2-D conditions.

Although fluid flow becomes more two dimensional as the substrate/fluid thermal conductivity ratio increases, heat transfer

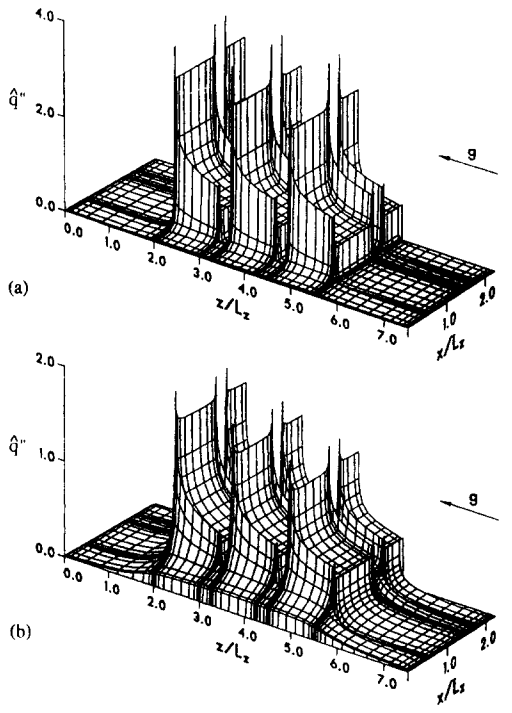

Figure 6 Local dimensionless heat flux distribution at the solid/fluid interface for $Ra^*_{L_z} = 10^8$: (a) Pr = 5.0, $R_h = 650$, $R_s = 0.48$ (water); (b) Pr = 25, $R_h = 6420$, $R_s = 4.7$ (FC-77); note the orientation of the gravity vector

is still influenced by 3-D edge effects of the discrete heat sources, as well as by thermal spreading in the x-direction. However, because the definition of the local Nusselt number is obscured by

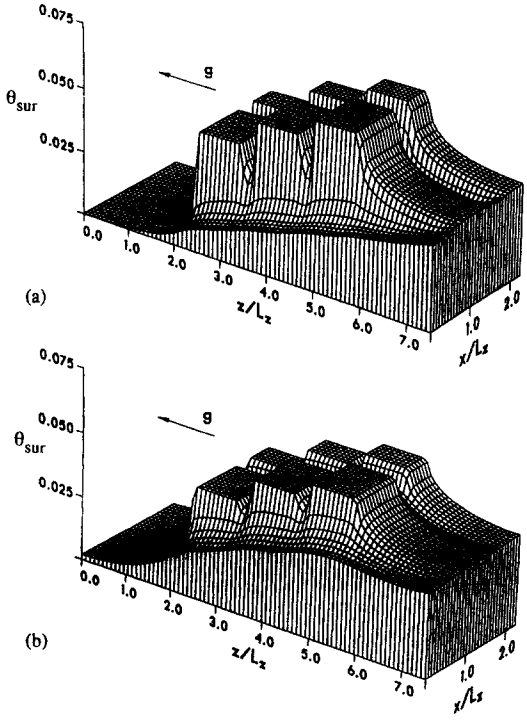

Figure 7 Local dimensionless temperature θ distribution at the solid/fluid interface for $Ra^*_{L_z} = 10^8$: (a) Pr = 5.0, $R_h = 650$, $R_s = 0.48$ (water); (b) Pr = 25, $R_h = 6420$, $R_s = 4.7$ (FC-77); note the orientation of the gravity vector

conjugate effects (Kim and Viskanta 1984), it is difficult to quantify 3-D conditions in terms of local Nusselt number profiles at the solid/fluid interface, which is neither isoflux nor isothermal.

To address conjugate heat transfer effects, a dimensionless local heat flux is defined at the solid/fluid interface:

$$\hat{q}'' = \frac{q''|_i}{q''} \tag{22}$$

where $q''|_i$ is the local, interfacial heat flux. The distribution of $\hat{q}''$ along the interface is shown in Figure 6 for both the water and FC-77 simulations (note the orientation of the gravity vector). Large variations in $\hat{q}''$ are apparent near the heater/substrate interfaces. The enhancement in $\hat{q}''$ at the leading edge of each heater in the first and second heater rows is caused by partial dissipation of the thermal boundary layer in the substrate region between heater rows and renewal of thermal boundary layer development at the heater leading edge. Substantial enhancement in $\hat{q}''$ along the lateral edges of each heater is caused by spanwise diffusion from the warm fluid over each heater surface to the relatively cool fluid in adjoining substrate regions. Because thermal spreading decreases with decreasing R_s, values of $\hat{q}''$ are larger for water (Figure 6a) than for FC-77 (Figure 6b). Increasing R_s to 4.7 in the FC-77 simulations increases thermal spreading through the substrate, thereby increasing $\hat{q}''$ in this region, with an accompanying decrease in $\hat{q}''$ at the heater locations.

The effect of thermal spreading on the local dimensionless temperature distribution at the solid/fluid interface is shown in Figure 7. Both conjugate simulations predict nearly isothermal conditions at the heater/fluid interface due to the high value of R_h. Temperatures are equivalent for heaters in each row, but increase from row three to row one because of a decrease in the convection coefficient and an increase in the local bulk fluid temperature. The spanwise uniformity in the temperature distribution breaks down at the heater edges because of the existence of significant spanwise diffusion. The temperature of the substrate increases from the cavity bottom ($z/L_z = 0$) to the cavity top ($z/L_z = 7.5$) because of an increase in the local bulk fluid temperature. The water simulations (Figure 7a) predict higher heater and lower substrate dimensionless temperatures because of the significant amount of energy passing through each heat source. With increasing R_s (Figure 7b), the amount of energy passing through the heaters decreases, while the amount entering the substrate increases. Hence, the dimensionless temperatures of the heater and substrate regions decrease and increase, respectively.

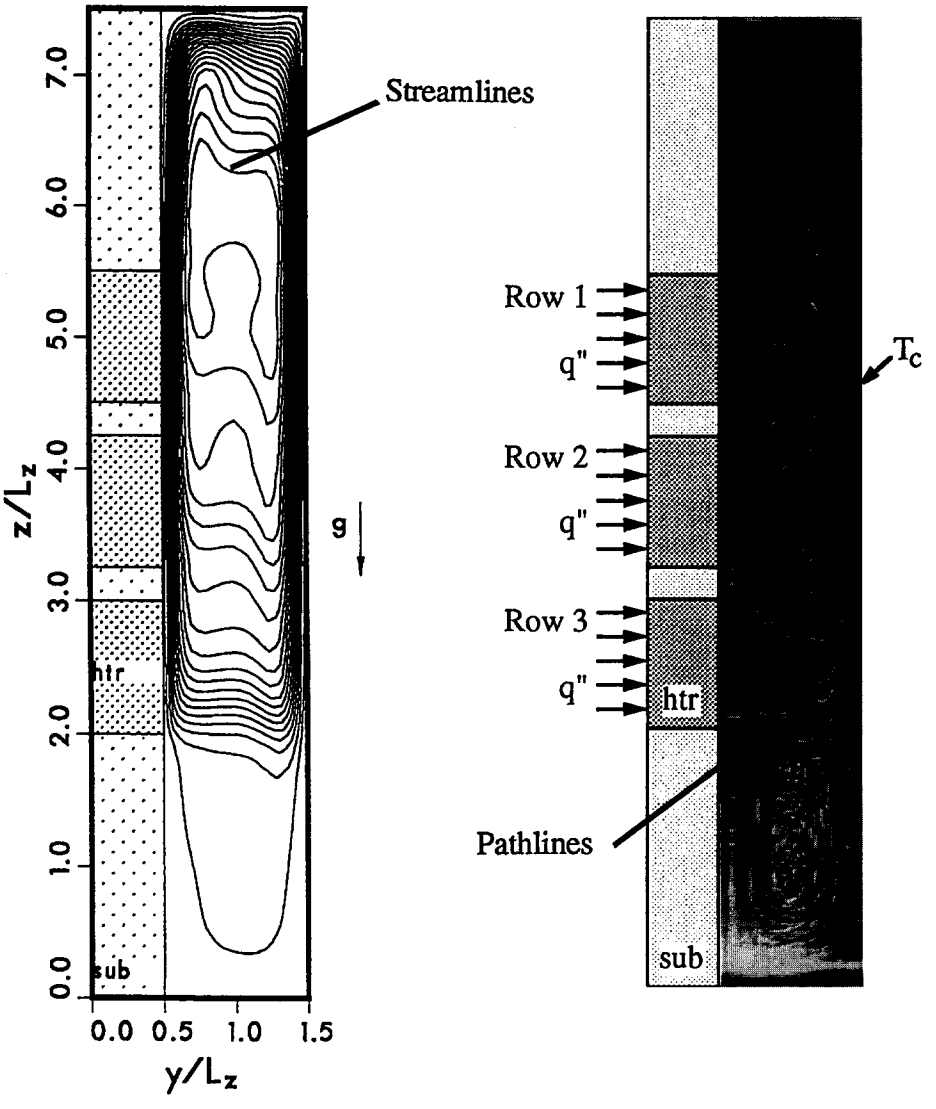

Figure 8 Streamlines predicted by the 2-D conjugate model for Pr = 5 and $Ra^*_{L_z} = 10^7$ and pathlines experimentally obtained in water for $Ra^*_{L_z} \approx 10^7$ and $x/L_z \approx 2.25$

The 2-D conjugate model predicts similar variations of $\hat{q}''$ and θ_{sur} in the z-direction, but obviously, it is unable to capture any of the spanwise diffusion effects displayed in Figures 6 and 7.

Comparisons to experimental data

Flow visualization was used to determine flow patterns qualitatively within the discretely heated cavity, and results were compared to those predicted numerically. A dimensionless stream function can be defined in the 2-D model as follows:

$$V = \frac{\partial \Psi}{\partial Z} \qquad W = -\frac{\partial \Psi}{\partial Y} \tag{23}$$

A similar parameter does not exist for the 3-D predictions. Figure 8 compares streamlines from the 2-D conjugate simulation for

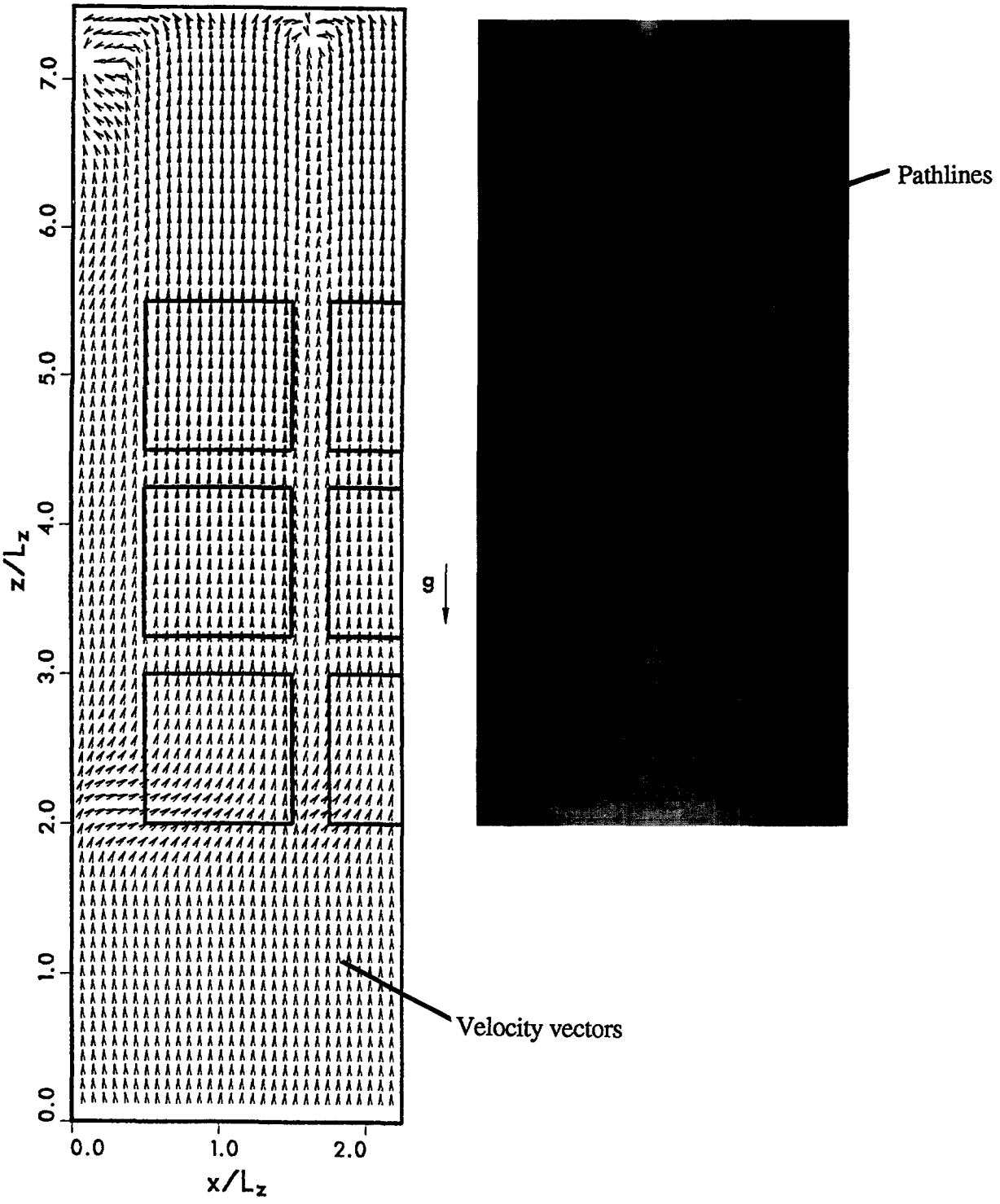

Figure 9 Velocity vectors predicted by the 3-D conjugate model for Pr = 5, $Ra^*_{L_z} = 10^7$, and $y/L_z - S_s/L_z = 0.2$ and pathlines experimentally obtained in water for $Ra^*_{L_z} \approx 1.2 \times 10^7$ and $y/L_z - S_s/L_z \approx 0.2$

water at $Ra^*_{L_z} = 10^7$ to the flow patterns obtained using pliolite particles in water at $Ra^*_{L_z} \approx 10^7$ and $x/L_z \approx 2.25$ (the cavity midplane). Agreement between the numerical and experimental results is excellent. Although most of the fluid traverses the cavity from the cold to the hot wall near row three, both the streamlines and pathlines indicate some fluid penetration into the lower cavity region. Predicted and observed flow patterns near the top of the cavity and along the cold wall are also in excellent agreement.

A clear cold plate was used for flow visualization with water in the X–Z plane. Figure 9 displays the vector field 2.54-mm from the heated wall ($y/L_z - S_s/L_z = 0.2$) in terms of predictions based on the 3-D conjugate model at $Ra^*_{L_z} = 10^7$ and pathlines observed for $Ra^*_{L_z} \approx 1.2 \times 10^7$. Deviations from two-dimensionality are evident near the bottom edge of row three as well as near the top of the cavity. In the numerical simulation, rising thermal plumes coincident with the heater columns impinge on the ceiling, bifurcate, and turn toward the cold plate, resulting in counter-rotating, helical flows confined to regions between the heater columns at the top of the cavity. Additional X–Z vector plots at other locations reveal that the counter-rotating cells persist past $y/L_z - S_s/L_z = 0.5$.

The photograph of particle pathlines in the experiment confirms the general features of the predicted flow field. The flow appears to be mainly 2-D, but 3-D effects are noticeable near the bottom edge of row three and at the top of the cavity.

The average temperature difference between each heater and the cold plate is shown in Figure 10 as a function of the applied power, where $\overline{T}_{sur,(i,j)}$ refers to the heater located in row i and column j (heater (1, 2) is indicated in Figure 1). Data for water are compared with 2- and 3-D predictions to assess the accuracy of the conjugate models. The data reveal negligible column-to-column variations in the measured values, which was confirmed by the 3-D model. The predictions were obtained for heat fluxes up to 8.33 W/cm^2, corresponding to $Ra^*_{L_z} = 10^8$.

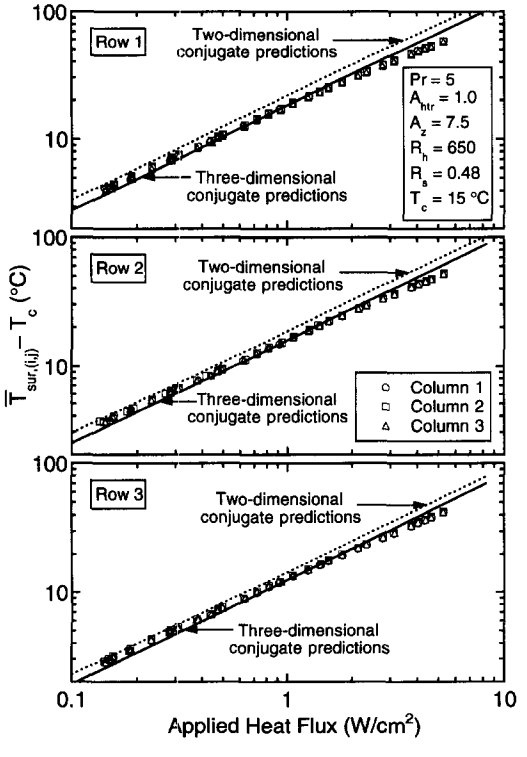

Figure 10 Comparisons of measured average heater temperature differences for water with conjugate predictions for Pr = 5, R_h = 650, and R_s = 0.48

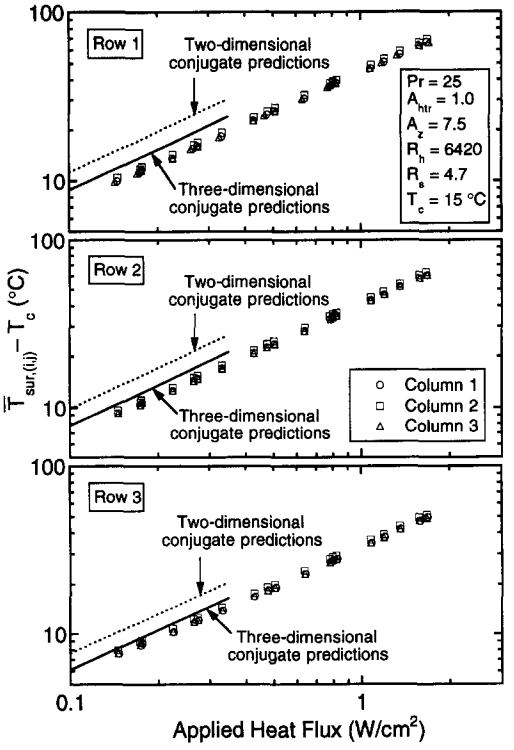

Figure 11 Comparisons of measured average heater temperature differences for FC-77 with conjugate predictions for Pr = 25, R_h = 6420, and R_s = 4.7

Excellent agreement is obtained between the 3-D conjugate predictions and the data, while the 2-D conjugate predictions exceed those of the 3-D model by 10–15%. Differences are due to heat transfer enhancement from edge effects and thermal spreading in the x-direction, both of which are neglected in the 2-D model. However, the 2-D predictions are still in good agreement with the data, because actual thermal spreading in the x-direction is constrained by the relatively low substrate/fluid thermal conductivity ratio ($R_s = 0.48$) and the small substrate region adjacent to the heater columns.

When FC-77 is the coolant, the increase in R_s to 4.7 enhances thermal spreading in the x-direction, and the 2-D conjugate predictions of the average surface temperature are about 20% higher than those predicted by the 3-D conjugate model (Figure 11), which are in good agreement with the data. An applied heat flux of $q'' = 0.35$ W/cm^2 corresponds to $Ra^*_{L_z} = 10^9$, and numerical predictions were not obtained for larger modified Rayleigh numbers. Although the 2-D model overpredicts the heater surface temperatures, it does predict the general trends with significantly reduced computational requirements.

Conclusions

Three-dimensional effects can have a discernible influence on fluid flow and heat transfer within a discretely heated cavity. While the fluid flow adjacent to the heaters is noticeably 3-D, the effect of discrete heating on local heat transfer is very substantial. Large spikes in the local heat flux are predicted near the edges of each heater, especially at low values of R_s. With increasing R_s, the high heat fluxes near the edges of the heaters are smoothed out by substrate conduction, which, in turn, leads to lower heater temperatures than those predicted by the 2-D model. With increasing R_s, fluid circulation begins to encompass the entire fluid cavity, and 2-D flow conditions are approached.

For the conditions of this study, the heater/fluid interface is isothermal, but heater temperatures vary from row-to-row. With increasing R_s, variations in the local dimensionless heat flux and temperature decrease along the solid/fluid interface, reducing the significance of local effects due to discrete heating. Flow visualization confirms the flow patterns predicted by the conjugate models, and 3-D conjugate predictions of the average surface temperature are in excellent agreement with experimental data. Although actual surface temperatures are overpredicted by the 2-D conjugate model, which does not consider thermal spreading in the x-direction, key trends are still captured by the model. Hence, because of its much smaller computational requirements, the 2-D model is well suited for predicting general trends associated with parametric variations (Heindel et al. 1995).

Acknowledgments

Support of this work by the National Science Foundation under Grant No. CTS-9004213 is gratefully acknowledged.

References

Bar-Cohen, A. 1991. Thermal management of electronic components with dielectric liquids. *Proc. ASME/JSME Thermal Engineering Joint Conference*, vol. 2, J. R. Lloyd and Y. Kurosaki (eds.) xv–xxxix

Bar-Cohen, A. 1993. Thermal management of electronic components with dielectric liquids. *JSME Int. J.*, **36**, 1–25

de Vahl Davis, G. 1983. Natural convection of air in a square cavity: A bench mark numerical solution. *Int. J. Num. Meth. Fluids*, **3**, 249–264

Fusegi, T., Hyun, J. M., Kuwahara, K. and Farouk, B. 1991. A numerical study of three-dimensional natural convection in a differentially heated cubical enclosure. *Int. J. Heat Mass Transfer*, **34**, 1543–1557

Heindel, T. J. 1994. A numerical and experimental study of three-dimensional natural convection in a discretely heated cavity. Ph.D. thesis, Purdue University, West Lafayette, IN

Heindel, T. J., Ramadhyani, S. and Incropera, F. P. 1995. Conjugate natural convection from an array of discrete heat sources: Part 2 — a numerical parametric study. *Int. J. Heat Fluid Flow*, **16**, 511–518

Hutchinson, B. R., Galpin, P. F. and Raithby, G. D. 1988. Application of additive correction multigrid to the coupled fluid flow equations. *Num. Heat Transfer*, **13**, 133–147

Hutchinson, B. R. and Raithby, G. D. 1986. A multigrid method based on the additive correction strategy. *Num. Heat Transfer*, **9**, 511–537

Incropera, F. P. 1988. Convection heat transfer in electronic equipment cooling. *J. Heat Transfer*, **110**, 1097–1111

Incropera, F. P. 1990. Liquid immersion cooling of electronic components. In *Heat Transfer in Electronic and Microelectronic Equipment*, A. E. Bergles (ed.), Hemisphere, New York, 407–444

Jaluria, Y. 1985. Natural convective cooling of electronic equipment. In *Natural Convection Fundamentals and Applications*, S. Kakac, W. Aung and R. Viskanta (eds.), Hemisphere, Bristol, PA, 961–986

Joshi, Y., Haukenes, L. O. and Sathe, S. B. 1993. Natural convection liquid immersion cooling of a heat source flush mounted on a conducting substrate in a square enclosure. *Int. J. Heat Mass Transfer*, **36**, 249–263

Kim, D. M. and Viskanta, R. 1984. Study of the effects of wall conductance on natural convection in differently oriented square cavities. *J. Fluid Mech.*, **144**, 153–176

Kline, S. J. and McClintock, F. A. 1953. Describing uncertainties in single-sample experiments. *Mech. Eng.*, **75**, 3–8

Patankar, S. V. 1978. A numerical method for conduction in composite materials, flow in irregular geometries, and conjugate heat transfer. *Proc. 6th International Heat Transfer Conference*, vol. 3, 279–302

Patankar, S. V. 1980. *Numerical Heat Transfer and Fluid Flow*. Hemisphere, Bristol, PA

Patankar, S. V. 1981. A calculation procedure for two-dimensional elliptic situations. *Num. Heat Transfer*, **4**, 409–425

Peterson, G. P. and Ortega, A. 1990. Thermal control of electronic equipment and devices. In *Advances in Heat Transfer*, vol. 20, J. P. Hartnett and T. F. Irvine Jr. (eds.), Academic Press, New York, 181–314

Polentini, M. S., Ramadhyani, S. and Incropera, F. P. 1993. Single-phase thermosyphon cooling of an array of discrete heat sources in a rectangular cavity. *Int. J. Heat Mass Transfer*, **36**, 3983–3996

Sathe, S. B. and Joshi, Y. 1991. Natural convection arising from a heat generating substrate-mounted protrusion in a liquid-filled two-dimensional enclosure. *Int. J. Heat Mass Transfer*, **34**, 2149–2163

Sathe, S. B. and Joshi, Y. 1992. Natural convection liquid cooling of a substrate-mounted protrusion in a square enclosure: A parametric study. *J. Heat Transfer*, **114**, 401–409

Wroblewski, D. and Joshi, Y. 1992. Transient natural convection from a leadless chip carrier in a liquid filled enclosure: A numerical study. In *Advances in Electronic Packaging — 1992*, EEP vol. 1-1, W. T. Chen and H. Abé (eds.), ASME Press, New York, 235–248

Wroblewski, D. E. and Joshi, Y. 1993. Computations of liquid immersion cooling for a protruding heat source in a cubical enclosure. *Int. J. Heat Mass Transfer*, **36**, 1201–1218

Wroblewski, D. E. and Joshi, Y. 1994. Liquid immersion cooling of a substrate-mounted protrusion in a three-dimensional enclosure: The effects of geometry and boundary conditions. *J. Heat Transfer*, **116**, 112–119